regolith build-up. In contrast, on a highly porous asteroid, only small impacts (perhaps $D < 1$ km for Mathilde) produce ejecta deposits outside the crater rim (like shot 1648), whereas blankets would be absent around large craters. Only a small amount of ejecta would escape Mathilde. Such asteroids would liberate significant meteoritic material only from catastrophic impacts that shatter and disperse the whole body.

High porosity does not guarantee formation of compaction craters. For example, dry sand has a porosity of 35%, but sand craters form primarily by excavation, with significant ejecta blankets at all sizes. Compaction in sand is minimal because it is already near a 'fully dense' state (the most efficient packing of particles). In this case, compaction cratering could only occur by crushing of the constituent sand grains, which requires stresses much higher than those experienced by most of the cratered material. Most granular silicate materials are at their fully dense state when their bulk density is in the range 2–3 g cm^{-3}. Thus, compaction cratering in silicates can only occur if the bulk density is well below ~2 g cm^{-3}. We note that large craters on the martian moons Phobos and Deimos (densities ~1.9 g cm^{-3}) do not show strong evidence of compaction effects[12], probably because they are close to the fully dense state. Furthermore, even initially highly porous asteroids about ten times larger than Mathilde's diameter would have lithostatic stresses comparable to the crush pressure of the material used here, and would naturally compact to near a fully dense state due to self-gravity. Therefore, compaction cratering is not expected to be common on large asteroids.

High porosity may even be a fleeting characteristic of Mathilde-sized asteroids. As shown by laboratory experiments[13,14], and by Mathilde, highly porous bodies can withstand multiple large impacts without disruption. Each impact locally compresses the asteroid, because its volume decreases by the crater volume, while all mass is retained. Formation of the five largest craters on Mathilde ($D_M > 20$ km), increased its bulk density by ~20%. Hence, Mathilde's initial density may have been even lower than the present value, especially considering that additional large craters may exist on the unobserved half of its surface. Over time, porous bodies may be compacted by impacts to the point of being fully dense. Ejection velocities would then increase, allowing escape of some debris and formation of ejecta blankets around large craters, much as we expect for compact, rocky bodies. □

Received 12 April; accepted 17 September 1999.

1. Veverka, J. *et al.* NEAR's flyby of 253 Mathilde: Images of a C asteroid. *Science* **278,** 2109–2112 (1997).
2. Housen, K. R., Schmidt, R. M. & Holsapple, K. A. Crater ejecta scaling laws: Fundamental forms based on dimensional analysis. *J. Geophys. Res.* **88,** 2485–2499 (1983).
3. Chapman, C. R., Merline, W. J. & Thomas, P. Cratering on Mathilde. *Icarus* (submitted).
4. Veverka, J. *et al.* NEAR Encounter with asteroid 253 Mathilde: Overview. *Icarus* (submitted).
5. Asphaug, E. *et al.* Disruption of kilometre-sized asteroids by energetic collisions. *Nature* **393,** 437–440 (1998).
6. Schmidt, R. M. & Holsapple, K. A. Theory and experiments on centrifuge cratering. *J. Geophys. Res.* **85,** 235–252 (1980).
7. Holsapple, K. A. & Schmidt, R. M. Point source solutions and coupling parameters in cratering mechanics. *J. Geophys. Res.* **92,** 6350–6376 (1987).
8. Holsapple, K. A. The scaling of impact processes in planetary sciences. *Annu. Rev. Earth Planet. Sci.* **21,** 333–373 (1993).
9. Housen, K. R., Schmidt, R. M. & Holsapple, K. A. Laboratory simulations of large scale fragmentation events. *Icarus* **94,** 180–190 (1991).
10. Kieffer, S. W. From regolith to rock by shock. *Moon* **13,** 301–320 (1975).
11. Feves, M., Simmons, G. & Siegfried, R. W. in *The Earth's Crust. Its Nature and Physical Properties* (ed. Heacock, J. G.) (Geophysical Monogr. 20, American Geophysical Union, Washington, DC, 1977).
12. Thomas, P. C. Ejecta emplacement on the martian satellites. *Icarus* **131,** 78–106 (1998).
13. Love, S. G., Hörz, F. & Brownlee, D. E. Target porosity effects in impact cratering and collisional disruption. *Icarus* **105,** 216–224 (1993).
14. Stewart, S. T. & Ahrens, T. J. Porosity effects on impact processes in solar system materials. Vol. 30,, CD-ROM (*Lunar Planetary Science Conference*, Houston, Texas, 1999).

Acknowledgements

This work was supported by NASA's Planetary Geology and Geophysics Program.

Correspondence and requests for materials should be addressed to K.R.H. (e-mail: kevin.r.housen@boeing.com).

Spatial sampling of crystal electrons by in-flight annihilation of fast positrons

A. W. Hunt*†, D. B. Cassidy*†, F. A. Selim‡, R. Haakenaasen§, T. E. Cowan†, R. H. Howell†, K. G. Lynn‖ & J. A. Golovchenko*¶#

* *Department of Physics, Harvard University, Cambridge, Massachusetts 02138, USA*
† *Lawrence Livermore National Laboratory, Livermore, California 94550, USA*
‡ *Engineering Physics Department, Alexandria University, Alexandria 21544, Egypt*
§ *Norwegian Defense Research Establishment, 2027 Kjeller, Norway*
‖ *Department of Physics, Washington State University, Pullman, Washington 99164, USA*
¶ *Division of Engineering and Applied Sciences, Harvard University, Cambridge, Massachusetts 02138, USA*
# *The Rowland Institute for Science, Cambridge, Massachusetts 02142, USA*

Energetic, positively charged particles travelling along a low-index crystal direction undergo many highly correlated, small-angle scattering events; the effect of these interactions is to guide or 'channel' (refs 1–8) the particles through the lattice. Channelling effectively focuses positive particles into the interstitial regions of the crystal: nuclear collisional processes such as Rutherford backscattering are suppressed, while the number of interactions with valence electrons increases. The interaction of channelled positrons with electrons produces annihilation radiation that can in principle[9–12] serve as a quantitative, spatially selective probe of electronic charge and spin densities within the crystal: in the interstitial regions, two-photon annihilation is enhanced relative to single-photon annihilation, because the latter process requires a nuclear recoil to conserve momentum. Here we report observations of single- and two-photon annihilation from channelled positrons, using a monoenergetic beam flux of 10^5 particles per second. Comparison of these two annihilation modes demonstrates the ability of channelled positrons to selectively sample valence electrons in a crystal. Useful practical implementation of the technique will require the development of more intense positron beams with fluxes approaching 10^7 particles per second.

These experiments were performed at the recently constructed 3-MeV monoenergetic positron beamline at Lawrence Livermore National Laboratory. An electrostatic accelerator was modified to accommodate a 109 mCi ^{22}Na positron source, a tungsten moderator, as well as appropriate focusing optics in the terminal. The positrons were accelerated to 2.65 MeV and then passed through two bending magnets, two solenoid focusing lenses and two quadrupole astigmatism correctors, all designed, constructed or modified for

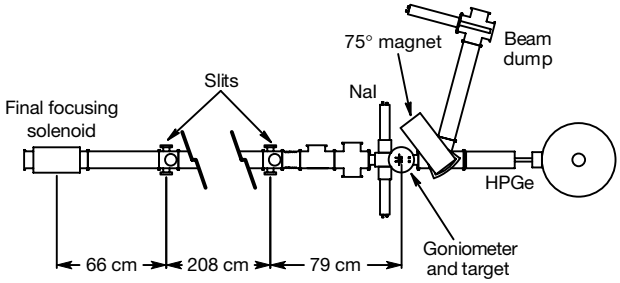

Figure 1 Experimental set-up. Shown is a diagram of the final leg of the 3-MeV monoenergetic positron beamline at Lawrence Livermore National Laboratory.

this experiment. The beam was then delivered to the stretch of optics shown in Fig. 1, where the channelling experiments were performed.

The positrons passed through a final solenoid focusing lens and a pair of collimation slits that defined the angular divergence and spatial size of the beam as it impinged on the target. Typical beam characteristics on target were 200,000 positrons per second in a spot 3 mm in diameter, with a maximum angular divergence of 0.25°. The energy spread of the beam was less than 0.4% of the full beam energy. The target was a 0.6-μm-thick free-standing gold crystal oriented in the ⟨110⟩ direction grown at the University of Aarhus with a surface minimum yield of 3% for 2 MeV α-particles. It was housed in a two-axis goniometer with a scintillator mounted on the front side. The scintillator had a hole 4.5 mm in diameter aligned with the target and was used for beam optimization and background subtraction.

A large-angle scattering scintillator was placed behind the target that detected positrons scattered between 10° and 20°. Further downstream a 75° bending magnet deflected the transmitted positrons to a well shielded beam dump. This was a specially designed double-focusing magnet with a 10° vertical and horizontal acceptance angle. Multiple scattering measurements and calculations predicted an angular divergence of half this value, ensuring efficient collection of the transmitted beam[13]. A scintillation detector used for normalization was positioned in the focal plane of the 75° magnet.

A multiple γ-ray spectroscopy system, consisting of a high purity germanium (HPGe) detector 7.3 cm in diameter and two 3-inch NaI scintillators, recorded annihilation photons from the gold crystal. The HPGe detector was placed in the forward direction 37.5 cm from the target and subtended a half angle of 5.6°. Annihilation photons with energies in excess of 3.3 MeV were constrained to emit in this forward cone by momentum conservation. The two NaI scintillators were placed on either side of the target chamber 8.9 cm in front of the target, collecting photons emitted between 142° and 163°. These detectors recorded the ~300 keV photons emitted in coincidence with the forward ~3.37 MeV γ-rays from two-photon annihilation. The signals from all detectors were routed to a multiple-parameter data acquisition system that recorded energy and time information for each detector on an event by event basis. Low background two-photon annihilation energy spectra were obtained by requiring a coincidence within 30 ns between the HPGe detector and one NaI scintillator. To identify single-photon annihilation events, a spectrum from the HPGe detector was collected concurrently with no coincidence requirement.

Figure 2 shows energy spectra obtained from the HPGe detector without (curve A) and with (curve B) the coincidence requirement. These particular demonstration spectra were obtained using a 3.6-μm-thick amorphous gold foil for enhanced statistics. In the single-photon annihilation process a monoenergetic γ-ray is emitted with the nucleus recoiling to conserve momentum. The energy of the photon, E_s, is given by

$$E_s = 2mc^2 + T_+ - |E_b|$$

where mc^2 is the rest mass energy of the electron, T_+ is the positron kinetic energy and E_b is the electron binding energy. Single photon annihilation is easily identified in curve A (that is, no coincidence required) of Fig. 2. The K-shell ($|E_b|$=81 keV), L-shell ($|E_b|$=13 keV) and M-shell ($|E_b|$=2.6 keV) annihilation events are seen at 3,591 keV, 3,659 keV and 3,670 keV respectively. The requirement of a nuclear recoil severely restricts this annihilation process to the most tightly bound electrons[14].

Two-photon annihilation does not require a nuclear recoil and can therefore occur with all electrons in the target material. The two emitted photons have energies that depend strongly on the emission angles. For 2.65-MeV positrons the photon energies range from 276 keV for 180° emission to 3,396 keV for 0° emission. The edge seen in Fig. 2 at 3,390 keV is from the most forward directed of these photons. By requiring a coincidence with the NaI scintillator the background is dramatically reduced and two-photon annihilation is clearly distinguished, as seen in curve B of Fig. 2. The peak at 3,370 keV is the signature of the forward-detected γ-rays from two-photon annihilation. The full-width at half-maximum of 46.6 keV is 6 times larger than the energy resolution of the HPGe detector and is determined by the kinematics of the two-photon annihilation process in conjunction with the angular acceptances of the detectors. The Compton edge at 3,130 keV and the continuous plateau at lower energy are due to γ-ray Compton scattering out of the HPGe detector. The small peak at 2,859 keV is the single γ-ray escape peak from recombining positron–electron pairs created in the detector. Both of these mechanisms allow valid two-photon annihilation events to be recorded below the peak at 3,370 keV. Including the events from ~1 MeV through the photo peak significantly improves the statistics in our channelling studies.

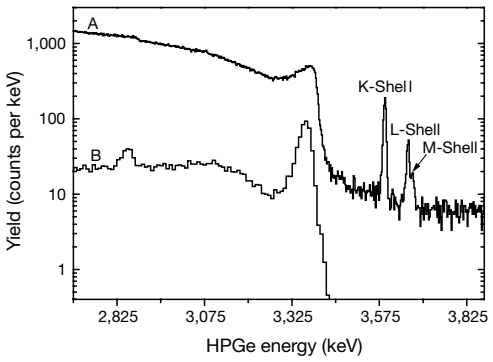

Figure 2 HPGe energy spectra. Annihilation radiation results from 2.65-MeV positrons impinging on a 3.6-μm polycrystalline gold foil. Curve A, no coincident photon required. Curve B, coincident photon required within 30 ns in one of the 3-inch detectors.

Using the scattering detector and spectra similar to those in Fig. 2, the angular yields from large-angle scattering, two-photon annihilation and K-shell one-photon annihilation were measured for positrons channelled through the 0.6-μm-thick gold crystal near a ⟨110⟩ axial direction. (With this crystal thickness, the positron flux was too weak to produce observable L-shell or M-shell one-photon annihilation signals.) The results are plotted in Fig. 3. The horizontal axis represents the angle between the positron beam and the ⟨110⟩ axis of the crystal. The vertical axis is the observed yield normalized to unity for a non-channelling direction. Each annihilation datum took at least 12 hours to accumulate. For scattered positrons the on-axis minimum yield is 6.5% and the full-width at half-minimum of the channelling dip is 1.65°. The on-axis reduction of large-angle nuclear scattering reflects the strong channelling suppression of the small-impact parameter collisions ($b < 4 \times 10^{-3}$ Å) required for deflection to occur into the scattering detector. The observed width is 8% below the calculated value of ~1.8° obtained from a dynamical diffraction yield calculation[3] which does not account for dechannelling processes. This calculation is based on a formalism that successfully describes the well known phenomenon of electron-channelling radiation[15]. Inclusion of dechannelling processes into the computation would improve the agreement but is a complex task.

The similarity between the channelling yield curves for K-shell annihilation and large-angle scattering may be understood by considering the K-shell Bohr radius ($a = 7 \times 10^{-3}$ Å), the scattering impact parameter ($b = 4 \times 10^{-3}$ Å) and the gold atomic thermal vibration amplitude (ρ = 0.12 Å). Since both processes require close proximity to the nucleus, smaller than the thermal vibration

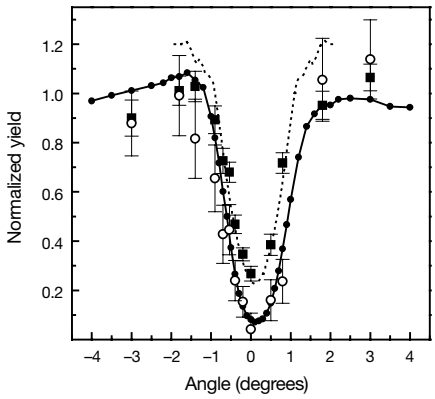

Figure 3 Normalized angular yield curves. Results are shown for 2.65-MeV positrons undergoing large-angle scattering (solid line with filled circle), single-photon annihilation (open circle) and two-photon annihilation (filled square). Angle on horizontal axis measured from the ⟨110⟩ axis of the 0.6-μm gold crystal. The dashed line is a dynamical diffraction yield calculation for two-photon annihilation including a dechannelling correction from the experimentally observed scattering minimum yield.

amplitude, they are expected to exhibit very similar channelling characteristics. In comparison, the sensitivity of two-photon annihilation to the outer and valence electrons causes a striking difference. The full width is reduced to 1.25 ± 0.09° and the minimum yield is four times higher at 27 ± 3%. This is unambiguously attributed to the extended nature of the electron clouds around the nuclei and the delocalized electrons in the interstitial region. Since the single-photon annihilation cross-section for these electrons is negligible, the smaller minimum yield of single- versus two-photon annihilation verifies that annihilation with the outer and valence electrons is enhanced by the channelling process.

Also shown in Fig. 3 is the dynamical diffraction yield calculation for two-photon annihilation. The electron densities and crystalline potential were calculated using a state-of-the-art augmented plane wave method[16]. The calculated full width agrees well with the two-photon annihilation data and the calculated minimum yield is 14.5% in the absence of dechannelling. Dechannelled positrons are not confined to the interstitial regions and consequently they may interact with the core electrons which increases the annihilation yield. From the observed scattering minimum yield we can estimate that dechannelling will increase the two-photon minimum yield to 23%, which is 1.5 standard deviations from the experimentally observed value. Using these calculations we can also estimate the valence-electron contribution. In gold, we consider the valence electrons to be the 10 electrons in the 5*d* shell and the electron in the 6*s* shell. At large incident angles, where channelling does not occur, positrons penetrate into all regions of the crystal and therefore sample all electrons equally. Since there are 11 valence electrons, they constitute 14% of the total sampled at large angles. In contrast, channelled positrons are focused into the interstitial region, where the valence electrons account for almost all of the electron density and their annihilation contribution increases to 56% at minimum yield with the experimentally observed dechannelling correction and background subtraction included. An implication of this enhancement is the potential to investigate charge density effects reflecting crystal bonding. For gold, our calculations predict a 3.5% increase in minimum yield for the case of a bonded crystal compared with a pseudo-crystal comprised of neutral unbonded atoms. This effect would be easily measurable with an increase in positron flux of 2 or 3 orders of magnitude.

Thus the enhanced minimum yield observed for two-photon over one-photon annihilation confirms our expectations that two-photon annihilation channelling effects would be very sensitive to electron densities in the interstitial regions of crystals. Indeed, the relative influence of valence electrons on channelling annihilation can be estimated to be about ten times larger than the relative contribution of valence electrons to low-order Fourier components of the charge density. These Fourier components are directly measured by X-ray diffraction techniques and have been used to determine electron densities in crystals[17,18]. These components have also been obtained by dynamical electron diffraction methods[19,20], which have an advantage over X-ray methods in that the core-electron contribution to the scattering is cancelled by the nuclear potential. The spatial probe provided by positron-annihilation channelling has an enhanced sensitivity to valence electrons that is determined by the positive charge of the probe. It would be interesting to determine whether a similar advantage exists for positrons in dynamical diffraction transmission studies.

If the positron-channelling phenomena revealed by this research are eventually to result in an accurate, easily applied probe of electrons in solid-state materials, it is clear that thinner crystals are required in order to reduce dechannelling effects and high positron-beam currents are needed in order to perform experiments on a practical timescale; monoenergetic MeV positron-beam currents greater than 10^7 positrons per second will be required. Stronger positron sources, improved moderators, polarization control, and more efficient detection and beam transport capabilities are possible with current technology. This new capability will also enable significant extensions of the experimental approach reported here. A next-generation beam facility will allow the development of practical atomic-scale channelling measurements of electronic spin densities[9–12], and momentum profiles in addition to valence and bonding electron density maps. We particularly look forward to the prospect of performing spin-density measurements on thin-film magnetic crystals ~1,000 Å in thickness. Similar measurements on such small samples are well beyond the capabilities of neutron diffraction techniques. □

Received 29 June; accepted 20 September 1999.

1. Lindhard, J. Motion of swift charged particles, as influenced by strings of atoms in crystals. *Phys. Lett.* **12,** 126–128 (1964).
2. Lindhard, J. Influence of crystal lattice on motion of energetic charged particles. *K. Danske Vidensk. Selsk. Mat.-fys. Medd.* **34**(14), 1–64 (1965).
3. Howie, A. Diffraction channeling of fast electrons and positrons in crystals. *Phil. Mag.* **4,** 223–237 (1966).
4. Uggerhøj, E. Orientation dependence of the emission of positrons and electrons from ^{64}Cu embedded in single crystals. *Phys. Lett.* **22,** 382–383 (1966).
5. Uggerhøj, E. & Andersen, J. U. Influence of lattice structure on motion of positrons and electrons through single crystals. *Can. J. Phys.* **46,** 543–550 (1968).
6. Andersen, J. U., Augustyniak, W. M. & Uggerhøj, E. Channeling of positrons. *Phys. Rev. B* **3,** 705–711 (1971).
7. Andersen, J. U., Andersen, S. K. & Augustyniak, W. M. Channeling of electrons and positrons. *K. Danske Vidensk. Selsk. Mat.-fys. Medd.* **39**(10), 1–58 (1977).
8. Schultz, P. J., Logan, L. R., Jackman, T. E. & Davies, J. A. Channeling effects on positron transmission through thin crystals. *Phys. Rev. B* **38,** 6369–6379 (1988).
9. Haakenaasen, R. *et al.* Quantum channeling effects for 1 MeV positrons. *Phys. Rev. Lett.* **75,** 1650–1653 (1995).
10. Hau, L. V. *et al.* On the role of classical and quantum notions in channeling and the development of fast positrons as a solid state probe of valence electron and spin densities. *Nucl. Instrum. Methods B* **119,** 30–41 (1996).
11. Hau, L. V., Hunt, A. W., Golovchenko, J. A., Haakenaasen, R. & Lynn, K. G. in *Proc. 11th Int. Conf. Positron Annihilation* (eds Jean, Y. C. Eldrup, M., Schrader, D. M. & West, R. N.) 119–123 (Trans Tech, Uetikon, Zuerich, Switzerland, 1997).
12. Haakenaasen, R. *et al.* in *Proc. 11th Int. Conf. Positron Annihilation* (eds Jean, Y. C. Eldrup, M., Schrader, D. M. & West, R. N.) 257-259 (Trans Tech, Uetikon, Zuerich, Switzerland, 1997).
13. Selim, F. A. *Penetration of Energetic Positrons through Crystalline and Noncrystalline Media*. Thesis, Alexandria Univ. (1999).
14. Palathingal, J. C., Asoka-Kumar, P., Lynn, K. G. & Wu, X. Y. Nuclear-charge and positron-energy dependence of the single-quantum annihilation of positrons. *Phys. Rev. A* **51,** 2122–2130 (1995).
15. Andersen, J. U., Bonderup, E., Lægsgaard, E., Marsh, B. B. & Sørensen, A. H. Axial channeling radiation from MeV electrons. *Nucl. Instrum. Methods* **194,** 209–224 (1982).
16. Rajagopal, A. K. in *Advances in Chemical Physics* (eds Prigogine, I. & Rice, S. A.) Vol. 41 (John and Sons, New York, 1980).
17. Dawson, B. The covalent bond in silicon. *Proc. R. Soc. Lond. A* **298,** 379–394 (1967).
18. Aldred, P. J. E. & Hart, M. The electron distribution in silicon. *Proc. R. Soc. Lond. A* **332,** 223–238 (1973).
19. Zuo, J. M., Kim, M., O'Keeffe, M. & Spence, J. Direct observation of d-orbital holes and Cu-Cu bonding in Cu_2O. *Nature* **401,** 49–52 (1999).

20. Zuo, J. M., O'Keeffe, M., Rez, P. & Spence, J. C. H. Charge density of MgO: Implications of precise new measurements for theory. *Phys. Rev. Lett.* **78,** 4777–4780 (1997).

Acknowledgements

We thank J. Chevalier, W. Gibson, R. A. Levesque, J. U. Andersen, M. Weinert and J. C. Palathingal for contributions to this research. This work was supported by the National Science Foundation, the Norwegian Research Council and the Department of Energy through Lawrence Livermore National Laboratory.

Correspondence and requests for materials should be addressed to J.A.G.

Diffusion mechanisms in metallic supercooled liquids and glasses

X.-P. Tang*, Ulrich Geyer†, Ralf Busch‡, William L. Johnson‡ & Yue Wu*

** Department of Physics and Astronomy, University of North Carolina, Chapel Hill, North Carolina 27599-3255, USA*
† Erstes Physikalisches Institut der Universität Göttingen, Bunsenstraβe 9, D-37073 Göttingen, Germany
‡ W.M. Keck Laboratory of Engineering Materials, California Institute of Technology, Pasadena, California 91125, USA

The mechanisms of atomic transport in supercooled liquids and the nature of the glass transition are long-standing problems[1–4]. Collective atomic motion is thought to play an important role[4–6] in both phenomena. A metallic supercooled liquid represents an ideal system for studying intrinsic collective motions because of its structural similarity to the "dense random packing of spheres" model[7], which is conceptually simple. Unlike polymeric and network glasses, metallic supercooled liquids have only recently become experimentally accessible, following the discovery of bulk metallic glasses[8–12]. Here we report a ^{9}Be nuclear magnetic resonance study of Zr-based bulk metallic glasses[8,9] in which we investigate microscopic transport in supercooled liquids around the glass transition regime. Combining our results with diffusion measurements, we demonstrate that two distinct processes contribute to long-range transport in the supercooled liquid state: single-atom hopping and collective motion, the latter being the dominant process. The effect of the glass transition is clearly visible in the observed diffusion behaviour of the Be atoms.

In the past few years, bulk metallic glasses with extraordinary glass-forming abilities have been discovered, such as $Zr_{41.2}Ti_{13.8}Cu_{12.5}Ni_{10}Be_{22.5}$ (Vit1; ref. 8) and $Zr_{46.75}Ti_{8.25}Cu_{7.5}Ni_{10}Be_{27.5}$ (Vit4; ref. 9). Their crystallization kinetics in the supercooled liquid state (SLS) is very slow compared to conventional metallic glasses[10], so that investigations of atomic transport in the metallic SLS become possible. For Vit1 and Vit4, the long-range atomic transport has been investigated by diffusion measurements[13–17]. It is, however, difficult to study atomic motion at microscopic scales in metallic systems. The conventional probes of local structural relaxation, such as dielectric measurement, are not applicable. For nuclear magnetic resonance (NMR), the difficulty arises from the fact that the relevant timescale of atomic motion near the glass transition is very long compared to the typical nuclear spin–lattice relaxation time (T_1) in metals. Fortunately, this is not the case for ^{9}Be NMR in Vit1 and Vit4 (T_1 is about 4 s at 300 K for ^{9}Be). It was shown recently[18,19] that the ^{9}Be spin alignment echo technique (SAE) is very effective in detecting Be hopping in glassy Vit1 and Vit4 with atomic jump rates as low as 0.1 s^{-1}.

Figure 1 shows the temperature dependence of the interdiffusion coefficients D of Be in Vit1 and Vit4. Below 620 K, which lies in the calorimetric glass-transition regime, Be diffusion shows Arrhenius behaviour with activation energies of about 1.1 eV in both alloys[13,14]. At higher temperatures, the temperature dependence of Be diffusion increases significantly, resulting in kinks in the Arrhenius plot of D. A kink has also been observed in $D(T)$ data for other elements, including Ni (ref. 15), B and Fe (ref. 16), and Co (refs 16, 17) in Vit4. One explanation of the observed kink suggests[15] that the diffusivity with larger activation energy above the kink temperature represents the intrinsic property of the SLS. The smaller activation energy below the kink temperature is attributed to an incomplete structural relaxation of the glassy state that would disappear after sufficiently long annealing. An alternative explanation[13] assumes that the observed low-temperature diffusion behaviour is an intrinsic property of the relaxed glassy state. Diffusion both above and below the kink temperature is attributed to hopping of single atoms of Be. This model explains the higher apparent activation energy above 620 K in terms of structural changes of the matrix in the SLS on the timescale comparable to the time interval between Be hopping events. It was assumed that such structural changes would enhance the probability of Be hopping and lead to increased diffusion[13]. Clearly, to elucidate the nature of atomic motion, information at the microscopic scale is needed.

The SAE technique[18–20] is based on the Jeener–Broekaert sequence $90°_x-\tau_1-45°_y-\tau-45°-\tau_2$, where 90° and 45° are the tipping angles of the radio-frequency pulses, x and y are the phases of the pulses, and τ_1, τ_2 and τ_3 are delays between pulses. Here the first two pulses with a short τ_1 (6–15 μs) create a pure quadrupole order, and a spin alignment echo is formed at $\tau_2 = \tau_1$ following the third pulse. Under the condition $\tau > T_2$ (the ^{9}Be spin–spin relaxation time T_2 is about 1.5 ms), the echo amplitude is proportional to the ensemble-averaged correlation function $f(\tau)=\langle\sin(\omega\tau_1)\sin(\omega'\tau_1)\rangle\exp(-\alpha\tau/T_1)$. Here α is a constant and is equal to 3 as measured in Vit1 and Vit4[18,19]. The frequencies ω and ω', varying over a range of $2\pi \times 100$ kHz in Vit1 and Vit4[19], are determined by the truncated quadrupole interactions experienced by the spin during τ_1 and τ_2, respectively[18–20]. The truncated quadrupole interaction with respect to the external magnetic field differs from site to site because of the disordered atomic structure of glasses and materials in a SLS. Thus, hopping of a Be atom is expected to change ω randomly within its range, and can be detected by the SAE technique through $f(\tau)$ decay. On the other hand, the SAE technique is not sensitive to collective motion involving Be atoms and most of their nearest neighbours. The truncated quadrupole interaction at the Be site changes very little under collective translation. This technique is also insensitive to constrained collective rotation with small rotation angle because $(\omega-\omega')\tau_1 \ll 1$. In both Vit1 and Vit4, a single-exponential

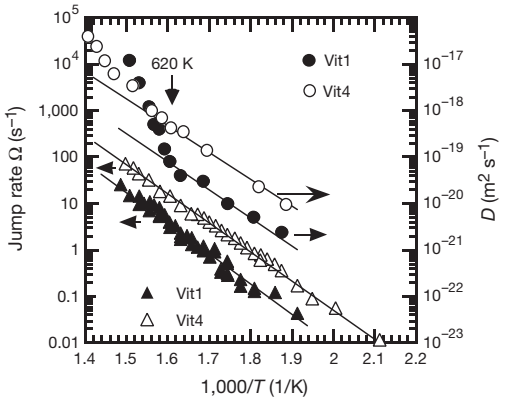

Figure 1 Elastic back-scattering of 6.5 MeV $^4He^{2+}$ ions and SAE measurements in bulk metallic glasses. The temperature dependence of Be diffusion coefficients D (measured by elastic back-scattering) and atomic jump rates Ω (measured by SAE) are shown for Vit1 and Vit4. D (scale on the right) and Ω (scale on the left) are plotted versus 1,000/T. A kink at 620 K, which is around the calorimetric glass-transition regime, is observed in the $D(T)$ curves in both Vit1 and Vit4. This kink is absent in the $\Omega(T)$ curves, which follow the same Arrhenius behaviour in both the SLS and glassy state.